Rotating convection-driven dynamos at low Ekman number

Jon Rotvig* and Chris A. Jones
School of Mathematical Sciences, University of Exeter, Exeter EX4 4QE, England
(Received 10 October 2001; revised manuscript received 18 July 2002; published 22 November 2002)

We present a fully 3D self-consistent convection-driven dynamo model with reference to the geodynamo. A relatively low Ekman number regime is reached, with the aim of investigating the dynamical behavior at low viscosity. This regime is computationally very demanding, which has prompted us to adopt a plane layer model with an inclined rotation vector, and to make use of efficiently parallelized code. No hyperdiffusion is used, all diffusive operators are in the classical form. Our model has infinite Prandtl number, a Rayleigh number that scales as $E^{-1/3}$ (E being the Ekman number), and a constant Roberts number. The optimized model allows us to study dynamos with Ekman numbers in the range $[10^{-5},10^{-4}]$. In this regime we find strong-field dynamos where the induced magnetic fields satisfy Taylor's constraint to good accuracy. The solutions are characterized by (i) a MAC balance within the bulk, i.e., Coriolis, pressure, Lorentz, and buoyancy forces are of comparable magnitude, while viscous forces are only significant in thin boundary layers, (ii) the Elsasser number is $O(10)$, (iii) the strong magnetic fields cannot prevent small-scale structures from becoming dominant over the large-scale components, (iv) the Taylor-Proudman effect is detectable, (v) the Taylorization decreases as the Ekman number is lowered, and (vi) the ageostrophic velocity component makes up 80% of the flow.

DOI: 10.1103/PhysRevE.66.056308 PACS number(s): 47.65.+a, 91.25.Cw

I. INTRODUCTION

Significant progress has been made in recent years in numerical simulations of the geodynamo. Self-consistent 3D models now produce dipole-dominated magnetic fields with strengths and reversals similar to the geomagnetic field. However, the numerically accessible part of parameter space is still quite far from the actual parameter values of planetary dynamos. In this paper we focus on the problems related to the low viscosity regime, which is the relevant limit for planetary dynamos. At present, 3D convection-driven dynamos in rotating spherical shells typically have Ekman numbers in the range $E \in [10^{-4},10^{-3}]$, e.g., Christensen *et al.* [1]. Viscosity still plays an important role in these solutions, so it is not clear whether they are in the correct dynamical regime, i.e., the leading order force balance in these models may not be the same as the leading order force balance in planetary interiors. Narrowing the investigated part of parameter space and reducing the integration time to a small fraction of the magnetic diffusion time may allow Ekman numbers below 10^{-4}. In comparison, a 3D plane layer model offers a more cost-reduced and efficient code, mainly because Cartesian geometry codes make effective use of fast Fourier transforms in all three dimensions. It is then possible to investigate the next decade $E \in [10^{-5},10^{-4}]$. Glatzmaier and Roberts [2] made one of the first attempts to circumvent the difficulties at low viscosity by use of hyperviscosity. This modified viscosity operator enhances diffusion monotonically as a function of the latitudinal wave number. Later, Zhang and Jones [3] showed that hyperviscosity has significant dynamical effects, broadening the convection cells as higher classical viscosity would do. Hyperviscosity can also prevent the dynamo from reaching solutions satisfying Taylor's constraint at low Ekman number, see Sarson *et al.* [4]. Thus it seems that the present implementations of hyperviscosity are of limited value when investigating low viscosity features of convection-driven dynamos. In this paper we use the classical form for all diffusion terms.

This paper considers nonmagnetic convection, convection-driven kinematic dynamos, and fully self-consistent dynamos at low Ekman number. It is organized as follows. A model description is given in Sec. II. In Sec. III we consider the properties of low Rayleigh number nonmagnetic convection. Based on the nonmagnetic bifurcation scheme, we select in Sec. IV a number of points in parameter space for the full dynamo problem. The dynamo results are described in Sec. V. Section VI gives our conclusions.

II. THE MODEL

An incompressible electrically conducting fluid is bounded by two horizontal plates. The distance between the plates is d. We impose d periodicity in the horizontal (x,y) directions, i.e., we may depict the layer as a box, Fig. 1. Nonslip boundary conditions are imposed on the velocity. Gravity $\mathbf{g}$ is uniform and directed vertically downwards. The system is heated from below keeping a temperature difference ΔT_b between the plates. Solid electrical insulators are imposed outside the layer. The rotation axis of the system $\mathbf{\Omega}=\Omega \mathbf{e}_{ra}$, where $\mathbf{e}_{ra}=(0,-\sin\theta,\cos\theta)$, is tilted relative to vertical by an angle θ in the (y,z) plane. The inclined rotation axis may be considered as an attempt to model a nonpolar region of the earth's outer core. For zero inclination, the system is (x,y) symmetric. A consequence is the existence of the Küppers-Lortz instability of finite-amplitude convection where the axis of the dominating convection roll continually rotates about the z axis. Recent work on this instability may be found in Ref. [5]. Inclining the rotation axis sufficiently eliminates this instability. This reduces the need of high resolution along the convection rolls, so that a 2.5D model (see Sec. III B below) can be used to explore

*Electronic address: jonr@maths.ex.ac.uk

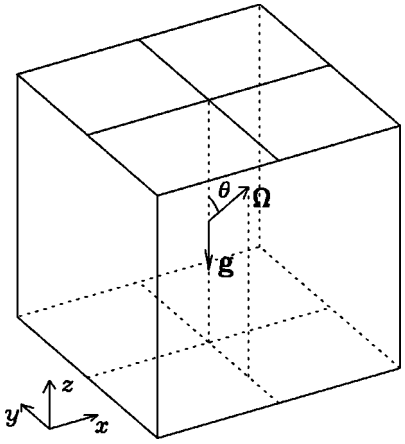

FIG. 1. A rotating cube of liquid made up of electrically conducting material. A Cartesian coordinate system is fixed relative to the box. The coordinate origin is at the box center, and the coordinate directions are indicated by the vector triplet.

parameter space alongside fully 3D runs. On the other hand, increasing θ towards $\pi/2$ for $E \leqslant 1\times10^{-4}$ causes the flow at onset of convection to become increasingly poloidal. At the sigular point $\theta=\pi/2$ the flow is purely poloidal. At $\theta=\pi/2.1$ no kinematic dynamos have been found for moderate Rayleigh and Roberts numbers; see also Sec. IV. As a compromise between these two extremes, we choose $\theta=\pi/4$, where the marginal flow at $E=1\times10^{-4}$ has equipartion between the toroidal and poloidal energies.

In the Boussinesq approximation, we then solve

$$\mathbf{e}_{ra}\times\mathbf{u} = -\nabla\phi + (\nabla\times\mathbf{B})\times\mathbf{B} + q\mathrm{Ra}T\mathbf{e}_z + E\nabla^2\mathbf{u}, \quad (1a)$$

$$\frac{\partial\mathbf{B}}{\partial t} = \nabla\times(\mathbf{u}\times\mathbf{B}) + \nabla^2\mathbf{B}, \quad (1b)$$

$$\frac{\partial T}{\partial t} + \mathbf{u}\cdot(\nabla T - \mathbf{e}_z) = q\nabla^2 T, \quad (1c)$$

$$\nabla\cdot\mathbf{u} = 0, \quad \nabla\cdot\mathbf{B} = 0, \quad (1d)$$

where the temperature T_b+T has been decomposed into the basic state profile $T_b(z)=-z-1/2+T_b(-1/2)$ and perturbation T. At the boundaries $T(x,y,\pm1/2)=0$. The velocity is denoted by $\mathbf{u}$, the magnetic field by $\mathbf{B}$, and ϕ is the sum of the pressure, the centrifugal potential, and the buoyancy potential of the basic state. In the following, ϕ is referred to as the pressure. We have nondimensionalized the system by choosing the following scales:

$$t: d^2/\eta, \quad \mathbf{r}: d, \quad \mathbf{u}: \eta/d, \quad \mathbf{B}: \sqrt{2\Omega\mu_0\rho\eta},$$
$$T_b, T: \Delta T_b, \quad \phi: 2\Omega\eta, \quad (2)$$

where (μ_0,ρ,η) are the vacuum permeability, density, and magnetic diffusivity, respectively. Thus in addition to the angle of inclination θ we introduce the Ekman, Rayleigh, and Roberts numbers

$$(E,\mathrm{Ra},q) = (\nu/2\Omega d^2, g\alpha\Delta T_b d/2\Omega\kappa, \kappa/\eta),$$

where (ν,κ) are the kinematic viscosity and thermal diffusivity, and α is the thermal expansion coefficient. The Rossby number $\mathrm{Ro}=\eta/2\Omega d^2$ estimates the strength of the inertial acceleration compared to the Coriolis force. For the geodynamo where $(\mathrm{Ro},E)=(10^{-6},10^{-15})$, it would be optimal to apply the magnetostrophic approximation (vanishing inertial acceleration and viscous forces), but inviscid self-consistent models have so far proven to be numerically intractable. In our model we put $\mathrm{Ro}\equiv0$ but retain kinematic viscosity. The Prandtl number $\mathrm{Pr}=E/q\mathrm{Ro}$ is then infinite.

In units of $\mathrm{Ro}\,\Omega\rho\eta d^3$ and $\Omega\rho\eta d^3$, the kinetic and magnetic energies are simply $E_{kin}=\langle|\mathbf{u}|^2\rangle_{xyz}$ and $E_{mag}=\langle|\mathbf{B}|^2\rangle_{xyz}$, where $\langle\cdots\rangle_{xyz}$ denotes the volume average. We note that for $\mathrm{Ro}=0$, we cannot compare the dimensional kinetic and magnetic energy. The Elsasser number is in terms of the dimensional magnetic field defined by $\Lambda\equiv B_{dim}^2/2\Omega\mu_0\rho\eta$. Thus the Elsasser number may be estimated by the nondimensional magnetic energy, $\Lambda=B^2\approx E_{mag}$.

The system (1a)–(1d) is solved by expanding the solenoidal fields $\mathbf{u}$ and $\mathbf{B}$ in toroidal, poloidal, and mean field components

$$\mathbf{u} = \nabla\times V\mathbf{e}_z + \nabla\times\nabla\times W\mathbf{e}_z + \mathbf{U}, \quad (3a)$$

$$\mathbf{B} = \nabla\times G\mathbf{e}_z + \nabla\times\nabla\times H\mathbf{e}_z + \mathbf{F}. \quad (3b)$$

The mean fields $\mathbf{U}$ and $\mathbf{F}$ depend only on z, and have no component in the z direction. Equations for the velocity potentials are obtained by the z component of the curl and double curl of Eq. (1a). The resulting system is supplemented with nonslip boundary conditions. In a similar way, the time derivative of the the magnetic field potentials are found from the z component and the z component of the curl of Eq. (1b) together with electrically insulating boundary conditions. Equations for the mean fields are obtained by x-y averaging the horizontal part of Eqs. (1a) and (1b)

$$\cos\theta\,\mathbf{e}_z\times\mathbf{U} = \overline{\{(\nabla\times\mathbf{B})\times\mathbf{B}\}_h} + E\frac{\partial^2\mathbf{U}}{\partial z^2}, \quad (4a)$$

$$\frac{\partial\mathbf{F}}{\partial t} = \overline{\{\nabla\times(\mathbf{u}\times\mathbf{B})\}_h} + \frac{\partial^2\mathbf{F}}{\partial z^2}, \quad (4b)$$

and supplementing with nonslip and insulating boundary conditions, respectively. The subscript h indicates the horizontal part of the vector, and a bar denotes the x-y average. Four linear independent solutions to the homogeneous part of Eq. (4a) are $\mathbf{U}=(1,\pm_1 i)\exp\{\pm_2\sqrt{(\cos\theta/2E)}(1\mp_1 i)z\}$, where the third sign is opposite to the first sign. For nonslip (and stress-free) boundary conditions, $\mathbf{U}=\mathbf{0}$ is the unique solution to Eq. (4a) without forcing. Thus the mean velocity is induced by the Lorentz force. The mean velocity may have a uniform component $\langle\mathbf{U}\rangle_z$ (this is not the case for stress-free boundary conditions since the volume average of the Lorentz force is zero $\overline{\langle(\nabla\times\mathbf{B})\times\mathbf{B}\rangle_z}=0$). Finally, having determined $\mathbf{u}$, we may evaluate the pressure force $-\nabla\phi$ directly from Eq. (1a).

Numerical implementation

The program is a development of the code used by Jones and Roberts [5]. This classical pseudospectral collocation method expands potentials, mean fields, and temperature in horizontal Fourier components and vertical Chebyshev polynomials,

$$A(x,y,z)=\sum_{l=-(N_x-1)}^{N_x-1}\sum_{m=-(N_y-1)}^{N_y-1}\sum_{n=0}^{N_z-1+N_b^A}A_{lm}^{n}\times e^{i2\pi(lx+my)}T_n(2z), \tag{5}$$

where N_b^A is the number of boundary equations for the quantity A. The equations to be solved are then, for each Fourier component, written at N_z collocation points along the z axis. These are the roots of $T_{N_z}(2z)$. The factors of the nonlinear terms are evaluated in physical space by Fourier transforming the (x,y) dependence and Chebyshev transforming the z coordinate. The products are then transformed back to the horizontal spectral space and vertical collocation mesh. The final nonlinear contribution is found by Adams-Bashforth extrapolation. The time stepping is implemented by the Crank-Nicolson method. In the full dynamo problem, the time step is increased at regular points in real time and adjusted in case of numerical instability. We note that the inclined rotation axis results in a complex matrix to be inverted for each Fourier component in solving Eq. (1a). For more details on the numerical method, see Ref. [5] and Appendix B.

III. NONMAGNETIC CONVECTION

A. 3D model

As a first step we consider the onset of convection as a function of Ekman number. At low viscosity we expect thin viscous boundary layers with a thickness of order $E^{1/2}$, Greenspan [6]. In an attempt to estimate the number of collocation points needed to resolve the Ekman layers, we determine the z resolution at which the kinetic energy growth rate at marginal convection has converged to better than 1%. The result is shown in Fig. 2. For efficient fast Fourier transforms, the resolution is always taken as either a power of two or three times a power of 2. As E is reduced, a critical value of E is found at which the resolution is no longer adequate. These are the values of E at which jumps in $(N_z)_{min}$ occur in Fig. 2. This minimum z resolution is also sufficient to resolve the second bifurcation, see below, and gives an important hint how to choose the z resolution at moderate Rayleigh number. An estimate of the number of collocation points within the Ekman layer at $z=1/2$ is given by $N_b=\Sigma_{n=0}^{N_z-1}\exp\{-(1/2-z_n)/2\sqrt{E}\}$. Those collocation points z_n lying outside the boundary layer make a negligible contribution to N_b, whereas each collocation point lying well within the boundary layer contributes by nearly unity to the sum. The number N_b is displayed in Fig. 2 showing that approximately 2–3 collocation points are needed within the Ekman layer.

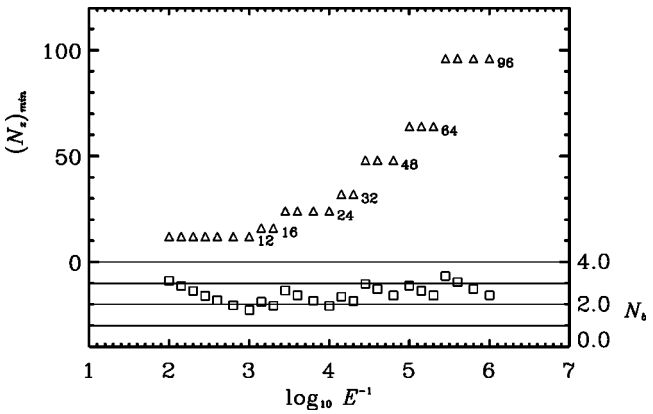

FIG. 2. Resolving the Ekman layers at the onset of convection. The required numbers of collocation points N_z along the z axis are shown by triangles. These numbers are also indicated by labels. The squares represent, on the right-hand scale, the corresponding number of collocation points N_b within an Ekman layer.

The critical Rayleigh number $\mathrm{Ra}_c^{(1)}$ for onset of convection appears to enter asymptotic regimes in the investigated range of Ekman number, see Fig. 3. In the high viscosity region, $E>1\times10^{-2}$, we find $\mathrm{Ra}_c^{(1)}=O(E)$, and for low Ekman number $E<1\times10^{-4}$, we observe as expected, Chandrasekhar [7], that $\mathrm{Ra}_c^{(1)}=O(E^{-1/3})$ [an alternative Rayleigh number $\widetilde{\mathrm{Ra}}=\mathrm{Ra}/E$, suitable for nonrotating convection, would of course result in the more familiar scalings $\widetilde{\mathrm{Ra}}_c^{(1)}=O(1)$ and $O(E^{-4/3})$ respectively].

We also show in Fig. 3 the l-index (wave number in the x direction) l_0 corresponding to the mode of largest amplitude. For $E>1\times10^{-3}$, the wave number $l_0=1$ dominates, so one convection roll fills the box. When $E<1\times10^{-3}$, the x scale of the convection becomes smaller than the box width, and it scales as $E^{1/3}$. The imposed periodic boundary conditions may be expected to have an effect on large-scale convection. Thus it is appropriate to stay well below $E<1\times10^{-3}$; ideally below $E<5\times10^{-5}$, where the horizontal plateaus of $l_0(E)$ have disappeared. In this regime the dominating y

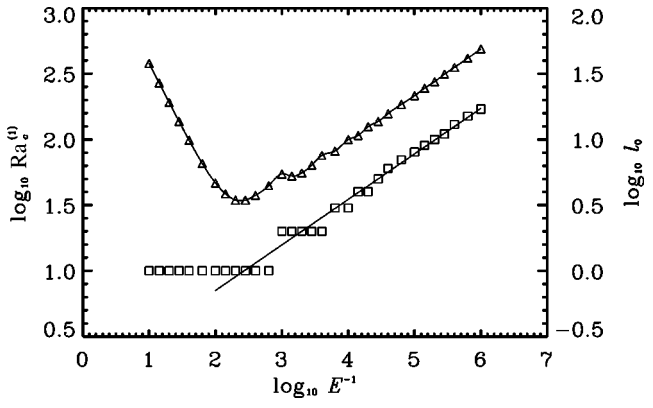

FIG. 3. Onset of convection. The triangles indicate $\mathrm{Ra}_c^{(1)}$ along the left-hand axis. The squares depict l_0 on the right-hand scale, where l_0 is the l index of the horizontal peak mode. Linear regression of the (E,l_0) points for $l_0\geqslant2$ results in the scaling $l_0=O(E^{-0.35})$.

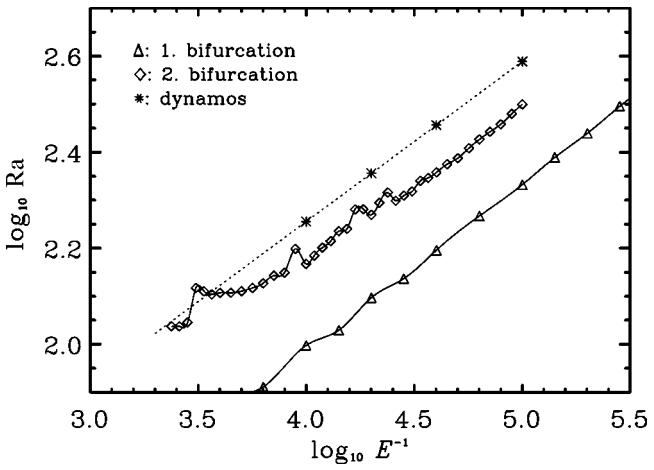

FIG. 4. The first two bifurcations of nonmagnetic convection. The triangles represent the critical Rayleigh number for onset of convection, $\mathrm{Ra}_c^{(1)}$. The diamonds indicate the points where the steady convection becomes unstable, $\mathrm{Ra}_c^{(2)}$. The four stars locate (E,Ra) of the dynamos considered in Sec. V. They are situated on the dotted line, which scales as $E^{-1/3}$.

mode of the steady convection is $m=0$. This is expected, because the Taylor-Proudman theorem requires that steady unforced inviscid motion should be independent of the rotation axis coordinate. Presence of this effect limits the *y* and *z* dependences. In our model buoyancy driven convection has to depend on the *z* coordinate, but a Taylor-Proudman effect in the *y* direction is simply maximized by the roll axis aligning with the *y* direction. The *z* structure is almost confined to the Ekman layers.

The critical Rayleigh number $\mathrm{Ra}_c^{(2)}$, where the steady convection becomes unstable, has been determined, Fig. 4. At this point two types of stable unsteady modes result. Depending on the Ekman number, the convection is either periodic or a two-torus. Fine structure in $\mathrm{Ra}_c^{(2)}$ is observed at $E=3.4\times10^{-4}, 1.1\times10^{-4}$, and 5.0×10^{-5}. We note that the large-scale structure of $\mathrm{Ra}_c^{(2)}$ is $O(E^{-1/3})$ for $E<3\times10^{-5}$. Thus compared with the onset of convection, the asymptotic behavior of the second bifurcation is only established at a lower Ekman number. However, the asymptotic scaling of the critical Rayleigh number is the same.

B. 2.5D model

In an attempt to reduce numerical costs further, we investigate how accurately a 2.5D model can reproduce the first two bifurcations of nonmagnetic convection. In general, the 2.5D approach is a drastic procedure to obtain lower numerical costs. In some cases it produces solutions quite different from the 3D case. The only way to justify the method is to compare the results with 3D solutions. A successful example may be found in Ref. [4]. A few models exist where the 2.5D approximation is exact, an example being the plane layer truncation of the G. O. Roberts dynamo. With roll cells parallel to the boundaries and 2D periodicity imposed in the layer, the magnetic field contains only a single mode along the roll cells.

Usually, 2.5D means that only two modes are retained in the half-dimensional direction, one mode of the form $\exp(i2\pi my)$ for some nonzero m together with the $m=0$ mode. Here we relax this definition. A 2.5D model may contain more than two modes in the *y* direction, but fewer than the number of modes needed to fully resolve the *y* direction. Our simulations show that a two-mode 2.5D model is insufficient to produce the correct low Rayleigh number bifurcation schemes. However, considering the location of the first and second bifurcations, a four-mode 2.5D model shows only minor deviations from the 3D scenario. This simplification is possible because the inclined rotation axis limits the amount of *y* dependence and this reduces the numerical costs considerably. It provides a powerful way of gaining approximated solutions before performing convergence tests at higher resolution. A further example will be given in the magnetic case.

IV. SELECTION OF DYNAMOS

The parameter values of the convection-driven dynamos below have been selected by the following arguments. The Rayleigh number is chosen with the same asymptotic scaling as for the first and second bifurcation of nonmagnetic convection, i.e., $\mathrm{Ra}=O(E^{-1/3})$. It would be optimal to consider only Ekman numbers $E<3\times10^{-5}$, but due to the high numerical cost in this regime, we include $E=1\times10^{-4}$ and 5×10^{-5}. At these points the relative distance of Ra to the first and second nonmagnetic bifurcations is approximately the same as when $E<3\times10^{-5}$, see Fig. 4. Thus we ensure that the dynamos are driven by the same relative forcing strength. To ease the numerical integration we want to keep the Rayleigh and Roberts numbers as small as possible. Thus we dispense with a highly supercritical Rayleigh number that would be needed to fully model the forcing of the geodynamo. On the other hand we want to ensure kinematic dynamo action at the chosen points in parameter space. The integration time is then determined by the need of good statistics rather than the question of persistent subcritical dynamo action. A subcritical plane layer dynamo at $E=5\times10^{-6}$ was reported by St. Pierre [8], which, however, made use of a perfect conducting exterior, hence preventing the magnetic energy from escaping through the upper and lower walls. Demonstration of subcritical dynamo action requires integration for several magnetic diffusion times, and this reduces the numerical advantage of low and subcritical values of (Ra,q). We found examples of initially promising subcritical 2.5D dynamos which, however, went into decay states after 1–2 magnetic diffusion times.

We consider the kinematic dynamo problem where the Lorentz force in Eq. (1a) has been neglected. We may then eliminate q in Eqs. (1a) and (1c) by the transformation $(\mathbf{u},\phi,t)\rightarrow(q\mathbf{u},q\phi,t/q)$. Thus the effect of retaining q is to enhance the velocity, pressure, and frequencies by a factor q. At $q=1$ the velocity field is determined for given Ra and E, and increasing q scales up the magnetic Reynolds number. For a subspace of (Ra,E), we therefore expect a critical Roberts number $q_c(\mathrm{Ra},E)$ above which dynamo action may occur. Figure 5 shows the result at $E=1\times10^{-4}$. Shortly

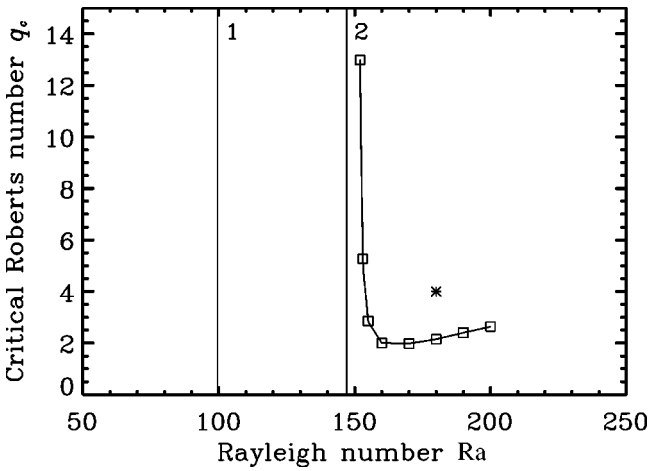

FIG. 5. The kinematic dynamo problem at $E=1\times10^{-4}$. The squares locate the critical Roberts number for onset of dynamo action. The vertical lines indicate the first and second bifurcations, of the nonmagnetic convection. The star represents the dynamo at $E=1\times10^{-4}$ in Sec. V.

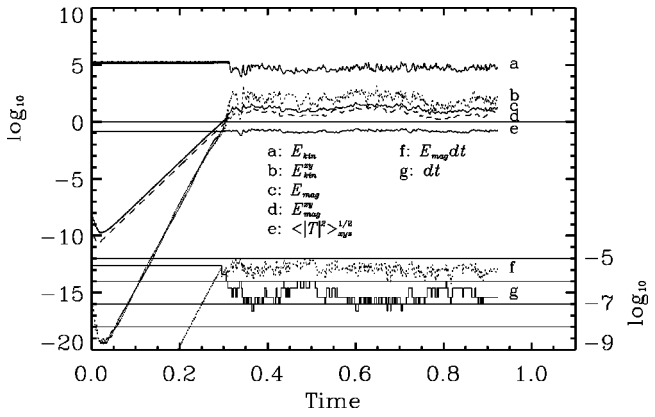

FIG. 6. The dynamo at $E=1\times10^{-4}$. Kinetic and magnetic energy, and temperature are displayed on the left-hand logarithmic scale. The time step dt and $E_{mag}\,dt$ are represented on the right-hand logarithmic scale. In order to define the linestyles, let us focus on the final state. From above we have kinetic energy (solid), energy of the mean velocity (dotted), magnetic energy (solid), energy of the mean magnetic field (dashed), temperature (first solid line below zero), time step multiplied by the magnetic energy (dotted), and the time step (solid).

after the second nonmagnetic bifurcation q_c may be determined. It displays a minimum value 2.0 at Ra=165.

Matthews [9] has considered the onset of kinematic dynamo action for simple rotating convection rolls. He finds that for moderate Ekman number and Prandtl number being unity, dynamo action can bifurcate directly out of the steady convection rolls, but at low Ekman numbers the flow is not a dynamo. This is consistent with our experience, which is that for $E<10^{-4}$, it is necessary (but not sufficient) for dynamo action to occur that convection is past the second bifurcation.

For the full dynamo problem we choose $(\mathrm{Ra},q)=(180,4)$. This point, which is reasonably far away from antidynamo regions, is the lowermost star in Fig. 4. Also the 2.5D flow is a dynamo at $(\mathrm{Ra},q)=(180,4)$. This point is located on the dotted line in Fig. 4, which scales as $O(E^{-1/3})$.

V. DYNAMO RESULTS

A. Kinematic and saturated regimes

The four dynamos at $(E,\mathrm{Ra})=(1\times10^{-4},180),(5\times10^{-5},227),(2.5\times10^{-5},286)$, and $(1\times10^{-5},388)$ are indicated by stars in Fig. 4. The numerical resolutions are $(N_x,N_y,N_z)=(24,16,32)$, (24,16,48), (32,24,48), and (32,24,64), respectively. The Taylor-Proudman effect implies that the y resolution can be lower than the x resolution. All dynamos have $\mathrm{Ra}=1.8\mathrm{Ra}_c^{(1)}$ and $q=4$. Being less numerically expensive, the dynamo solution at $E=1\times10^{-4}$ is developed from the kinematic regime, Fig. 6. The saturated solution is then successively propagated towards lower Ekman number. This set of runs, denoted as sequence I, is the one referred to below unless otherwise specified. The high numerical costs at the lower Ekman numbers allow only integration through a small fraction of a magnetic diffusion time. However, the integration time should be long enough to eliminate transients. Thus we adopt the snapshot approach taken by Roberts and Glatzmaier [10]. The solution is likely to be strongly time dependent on the time scale of magnetic diffusion. An advantage of the snapshot method is thus that the time dependence of the solution is moderate within the investigated time interval. We may argue in favor of the snapshot approach as follows. In the work of Brandenburg [11], a forcing term allows a clear distinction between large and small scales. He finds that small-scale components of the velocity and the magnetic field relax faster than the large-scale components. As shown later in the present paper, small-scale structures become increasingly important compared to the large-scale components at lower viscosity. Thus the snapshot method should capture a significant part of the relaxed solution.

The dynamo at $E=1\times10^{-4}$ is initiated by letting the nonmagnetic convection state develop and then adding a random seed magnetic field. After less than 0.05 magnetic diffusion times, the solution enters the kinematic regime where the magnetic field and the mean velocity induced by the magnetic field grow exponentially. The mean velocity never becomes an important part of the flow. For the saturated solution, the time-averaged ratio between the kinetic energy of the mean and total flow is 0.33%. At lower Ekman numbers this ratio stays small (0.36%,0.26%, and 0.10%, respectively). In contrast, the magnetic mean field plays a greater role, especially at higher Ekman number. The time-averaged ratio between the energy of the mean and total magnetic field is 41%, 36%, 34%, and 29%, respectively. Thus the magnetic mean field is an important part of the solution, but not, however, to the same extent as in the vertical rotation axis case [5] where the Küppers-Lortz instability provides an extra dynamo mechanism for magnetic mean field generation. We may note that the magnetic mean field becomes less important for low Ekman number.

As viscosity is reduced, we may hope to observe Ekman number scalings. As seen in Fig. 7, our example demonstrates that this is not likely to happen for $E>10^{-5}$. At E

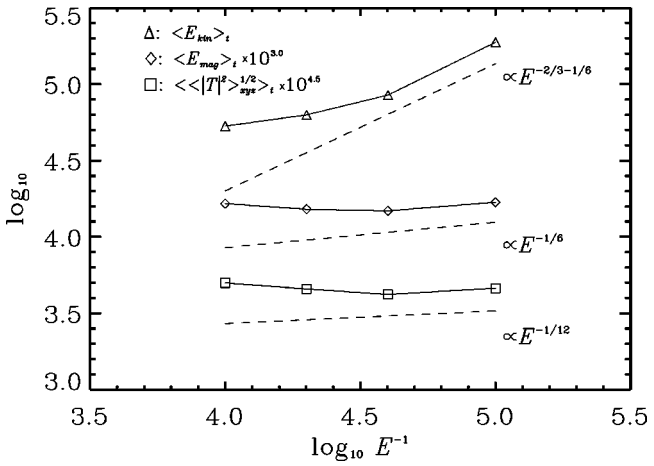

FIG. 7. Time-averaged kinetic energy (triangles), magnetic energy (diamonds), and temperature (squares) of the dynamos on a logarithmic scale. In order to obtain a compact figure we have displaced the magnetic energy and temperature by 3.0 and 4.5, respectively. The dashed lines visualize various scalings.

$=1\times10^{-5}$, we find that the kinetic energy increases as $O(E^{-5/6})$, while the magnetic energy $E_{mag}=O(E^{-1/6})$ and the root mean square of the temperature $\sqrt{\langle|T|^2\rangle}_{xyz}=O(E^{-1/12})$.

The required resolution of the saturated magnetic field is somewhat smaller than that of the kinematic solution. However, as seen in Fig. 6, the time step drops considerably in the saturated regime. Figure 8 shows that $\langle dt\rangle_t=O(E^{1+1/6})$, making the low Ekman number case very expensive. The time-averaged magnetic energy $\langle E_{mag}\rangle_t\in[15,17]$. The magnetic energy (Elsasser number) and the time step are anticorrelated, see Fig. 6. The quantity Λdt is relevant for the numerical stability of the magnetoconvection problem considered in the work of Walker *et al.* [12]. A stability condition in the infinite Prandtl number limit is shown to be $\Lambda dt<2E$. In Fig. 8 we observe that $\langle E_{mag}dt\rangle_t=O(E^1)$. At $E=1\times10^{-5}$, we find $\langle E_{mag}dt\rangle_t\approx2E/60$. Thus in comparison to the magnetoconvection problem, the full dynamo problem is considerably more expensive. It should be noted that the above scalings seem to be somewhat dependent on the magnetic energy. In a different sets of runs (sequence II), where $\langle E_{mag}\rangle_t\in[18,26]$ the time step has to be decreased further. We find that the scaling of $\langle dt\rangle_t$ and $\langle E_{mag}dt\rangle_t$ is multiplied by $O(E^{1/2})$.

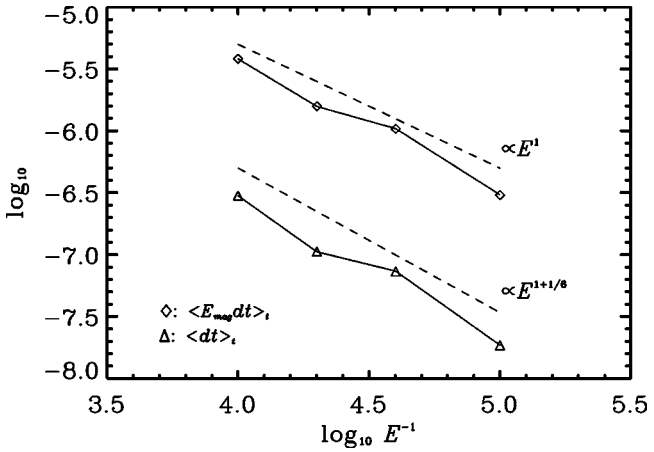

FIG. 8. Time-averaged time step of the dynamo integrations. The triangles and diamonds depict the time averages $\langle dt\rangle_t$ and $\langle E_{mag}dt\rangle_t$, respectively. The dashed lines visualize the indicated scalings.

B. Solution snapshots

All four dynamos display a strong influence of the Lorentz force on the flow. At high Ekman number the spatial scale of the flow in planes perpendicular to the rotation axis is determined by the viscous force. At lower viscosity we may expect the Lorentz force to increase the scale of the convection in regions where the magnetic field is strong and slowly varying.

Snapshots of nonmagnetic/magnetic energy spectra at the same point in parameter space are displayed in Fig. 9. The nonmagnetic convection is weakly oscillating. The sharp peaks in the spectrum are probably due to a (nontypical) perfect match between the periodic boundary conditions of our model and the periodicity of the corresponding solution in an infinite plane layer. At a slightly higher Rayleigh number, where the solution is steady, the spectral peaks broaden and structure has developed for odd m as well. We may compare the kinetic energy spectra of nonmagnetic/magnetic convection. In the two cases we observe that the dominating convective modes are $(l,m)=(\pm8,0)$ and $(\pm1,0)$, respectively. The results are summarized in Fig. 10. We find that the l index of the dominating velocity mode is strongly reduced by the Lorentz force for $E\leqslant5\times10^{-5}$. On the other hand, this scale separation effect is difficult to detect above $E>1\times10^{-4}$, where viscosity limits convection to large-scale structures. Various definitions of strong-field solutions have been suggested in the past. A review has recently been given by Zhang and Schubert [13]. They define a strong-field dynamo by the criterion that the magnetic feedback on the flow changes it significantly. This definition is more rigorous than to require a large value of the Elsasser number [which is $O(10)$ for all four dynamos]. However, it should be noted that also low-intensity magnetic fields can have a strong influence on the flow: as long as the Ekman number is sufficiently small, the magnetic field and rotation play the major role in controlling the length scales of the convection.

Figure 11 displays the spectral structure of the magnetic and kinetic energies in the (l,m) plane. The energy decline in the two directions may be described as follows. We denote the set of l indices by L and the positive l indices by L_+. Similar sets M and M_+ are defined for the m indices. We denote the energy of the (l,m) mode by $E(l,m)$ and put $E_{max}=\max\{E(l,m)|l\in L,m\in M\}$. The energy decline in the l directions over four orders of magnitude may then be described by $l(n),n=1,\ldots,8$, where

$$l(n)=\min\{l'\in L_+|E(l,m)\leqslant E_{max}10^{-n/2},$$

$$l\in L\backslash\{-(l'-1),\ldots,l'-1\},m\in M\}. \quad (6)$$

In the same manner we describe the energy decline in the m

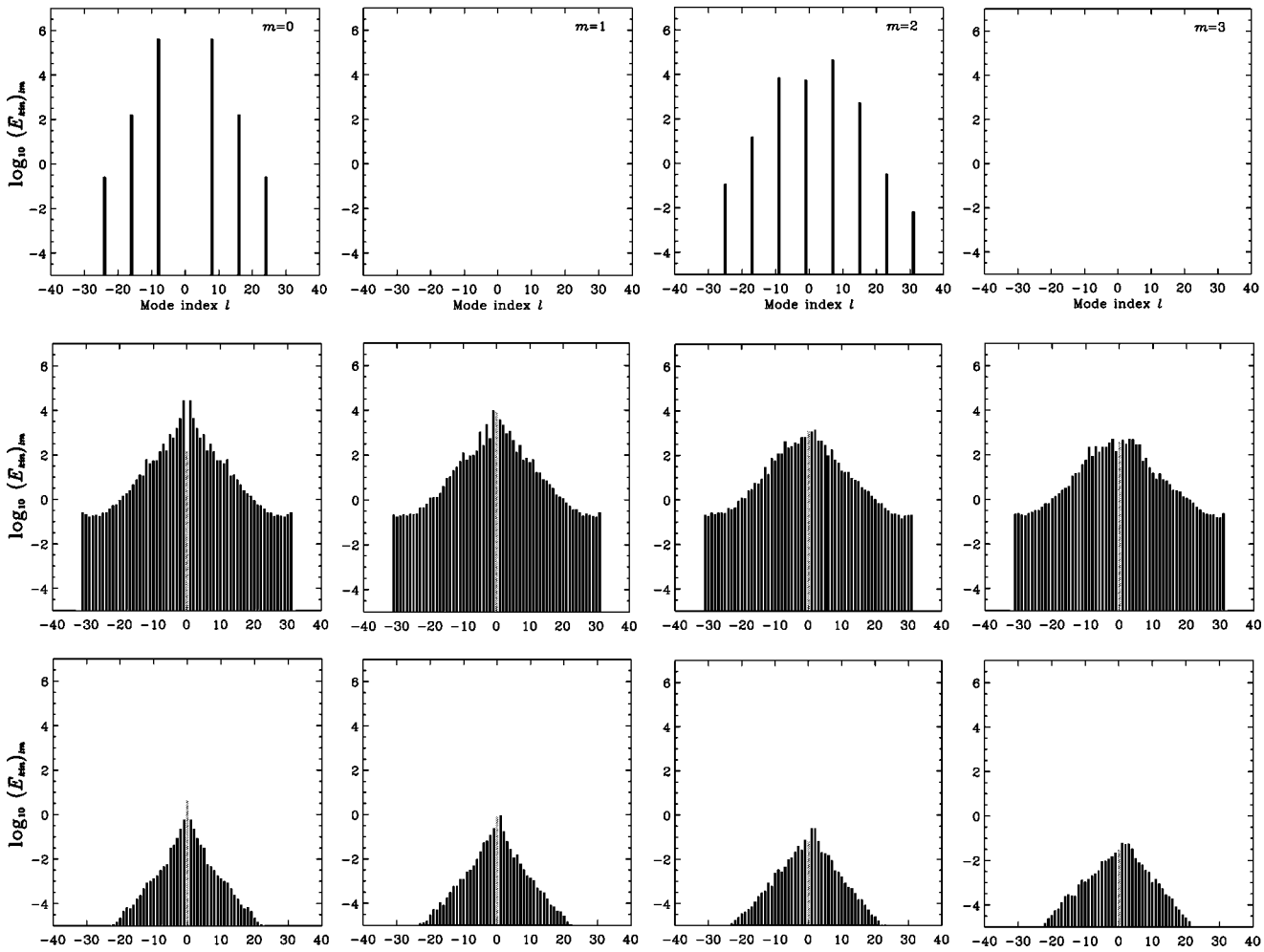

FIG. 9. Snapshots of kinetic and magnetic energy spectra. The first (second) row displays the kinetic energy spectra of nonmagnetic (magnetic) convection at the same point in parameter space, i.e., the location of the dynamo at $E=1\times10^{-5}$. The l spectra are shown for $m=0,1,2,3$. The third row displays the magnetic energy spectrum of the dynamo.

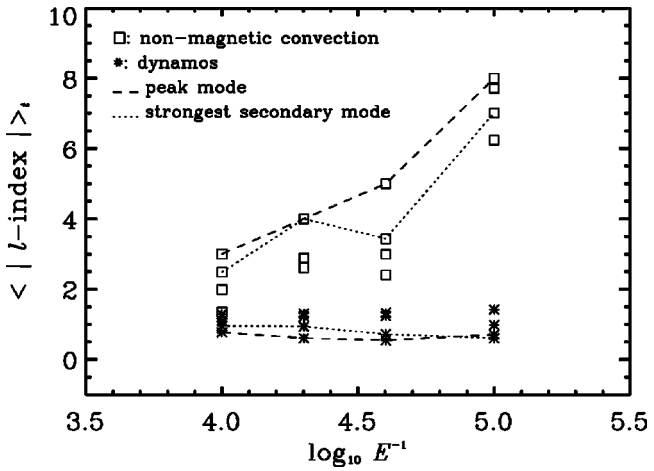

FIG. 10. The time-averaged l index of the four most significant (l,m) modes in the nonmagnetic (□) and the magnetic case (*). The peak modes are connected by dashed lines, and the strongest secondary modes by dotted lines.

direction by $m(n)$. Figure 11 shows that the l spectra are wider compared to the m spectra. As the Ekman number is lowered, the kinetic and magnetic energy spectra broaden. Thus despite the strong influence of the Lorentz force on the dominating l modes it clearly cannot prevent development of small-scale structures. We note that at $E=1\times10^{-4}$, the complexity of the small-scale part of the velocity increases faster than the complexity of the magnetic field, whereas for lower Ekman number similar complexity growth rates occur. This indicates that viscosity at $E=1\times10^{-4}$ still plays a significant role in determining the velocity length scales. At lower Ekman number the magnetic field takes over this role. In comparison with the velocity, the magnetic field is more large scale. This effect suggests that dynamo action in a moderate Rayleigh number regime mainly occurs on larger scales. By default, the nonmagnetic convection is a kinematic dynamo. Thus it seems that the influence of the Lorentz force on the flow switches off this small-scale dynamo and creates dynamo action at larger scales. This effect provides the first step towards subcritical dynamo action.

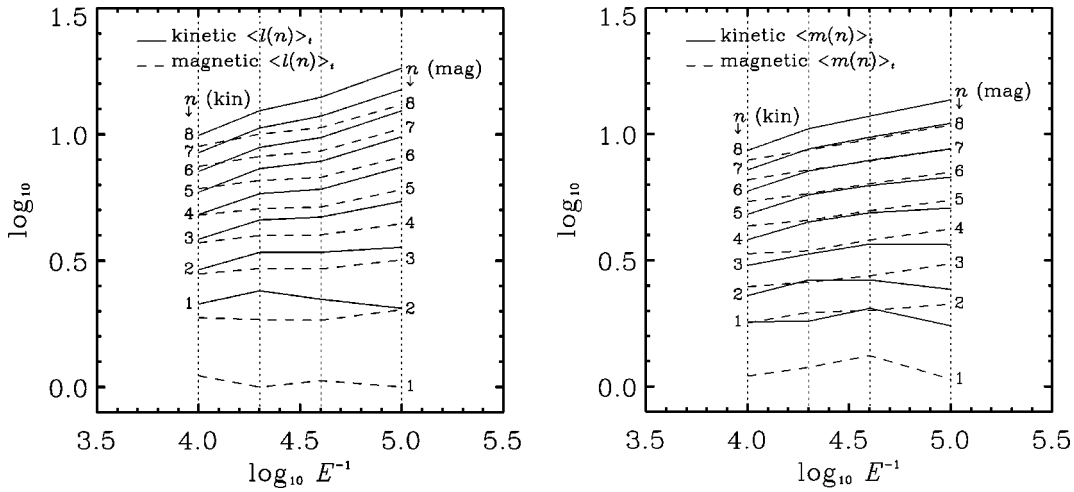

FIG. 11. Spectrum decay in the (l,m) plane. The left-hand panel displays the energy decline in the l index. The kinetic (magnetic) energy decline is shown by solid (dashed) lines. The time-averaged l index $\langle l(n)\rangle_t$, see text, is for fixed n plotted as function of the Ekman number. The value of n is indicated by labels, left(right)-hand sided labels belong to the solid (dashed) lines. The right-hand panel displays the energy decline in the m index in a similar way.

Figure 12 displays a snapshot of the velocity and magnetic field in the $y=0$ plane for the dynamo at $E=1\times10^{-5}$. We note the thin Ekman layers in u_x and u_y. In agreement with a strong Lorentz force we observe regions with large-scale convection. However, there are also regions where the flow resembles nonmagnetic convection with $O(E^{1/3})$ scales. Figure 13 shows the same quantities as Fig. 12 but in the $x=0$ plane. The relatively large scales in this plot are due to the effect of the inclined rotation axis. We clearly observe the Taylor-Proudman effect making the quantities less dependent on the rotation axis coordinate. A snapshot of the various forces in the $y=0$ plane is shown in Fig. 14. We see that for every force, except the viscous force, we may find more or less evenly distributed regions where the force is the strongest. The viscous force is strong only in the viscous boundary layers. In a similar snapshot for $E=1\times10^{-4}$ the viscous force plays a greater role in the bulk. Regions where the viscous force contributes with more than 6% are much more extended as compared to the $E=1\times10^{-5}$ case. In Fig. 15 we compare $|\mathbf{u}\times\mathbf{B}|$, $|\nabla\times\mathbf{B}|$, and $|\mathbf{B}|$ in the $y=0$ plane. We observe that $|\nabla\times\mathbf{B}|\ll|\mathbf{u}\times\mathbf{B}|$, indicating that the main balance in Eq. (1b) is between $\partial\mathbf{B}/\partial t$ and $\nabla\times(\mathbf{u}\times\mathbf{B})$, as in the frozen-flux approximation.

C. Estimation of Ekman number scalings

The results of the previous section suggest a MAC balance in Eq. (1a) outside the viscous boundary layers. Taking the curl in this region we obtain

$$-\frac{\partial\mathbf{u}}{\partial z_{ra}}=\nabla\times\{(\nabla\times\mathbf{B})\times\mathbf{B}\}+q\mathrm{Ra}\nabla\times T\mathbf{e}_z, \qquad (7)$$

where z_{ra} is the coordinate along the rotation axis. A balance between the terms in Eq. (7) results in estimates for typical velocities u and magnetic field length scales L_B. The Taylor-Proudman effect implies length scales of order $O(1)$ along the rotation axis. As seen in Figs. 12 and 13, this large-scale structure is also present in the buoyancy force. Let us assume that the temperature scales as $T=O(E^{\lambda_T})$. Balance between the first and last terms in Eq. (7) then gives a typical velocity $u\approx q\mathrm{Ra}T=O(E^{-1/3+\lambda_T})$. From Fig. 7 we may attempt to estimate $\lambda_T\approx-1/12$. The resulting kinetic energy $O(E^{-2/3+2\lambda_T})$ is consistent with Fig. 7. Let us assume that the magnetic field scales as E^{λ_B}. From a balance between the first two terms in Eq. (7) we may then estimate $L_B=B/\sqrt{u}=O(E^{1/6+\lambda_B-\lambda_T/2})$. Thus assuming a decreasing L_B as the viscosity is lowered, we find a lower limit on $\lambda_B>-1/6+\lambda_T/2$. Figure 7 suggests that $\lambda_B\approx-1/12$, so that $L_B=O(E^{1/8})$. This result is consistent with the observation that $|\nabla\times\mathbf{B}|\ll|\mathbf{u}\times\mathbf{B}|$. We have $|\nabla\times\mathbf{B}|/|\mathbf{u}\times\mathbf{B}|=O(E^{1/6-\lambda_B-\lambda_T/2})$. So as E is reduced, the leading order balance is the frozen-flux approximation. For the sequence II runs, we find $(\lambda_T,\lambda_B)\approx(-1/6,-1/12)$ when $E<5\times10^{-5}$. The above values of (λ_T,λ_B) should be taken as estimates. It is clear that numerical simulations, using today's typical computing facilities, only provide the first step towards determining the exact values of these numbers.

D. Taylorization

In the case of the geodynamo it seems appropriate to make the magnetostrophic approximation where the momentum equation reduces to

$$\mathbf{e}_{ra}\times\mathbf{u}=-\nabla\phi+(\nabla\times\mathbf{B})\times\mathbf{B}+q\mathrm{Ra}T\mathbf{e}_z. \qquad (8)$$

It is well known [14] that the existence of velocity solutions to Eq. (8) requires special forcings. Usually the solvability criterion reduces to a constraint on the magnetic part of the forcing. A Taylor state is defined to be a magnetic field that allows the momentum equation to be solved in the magnetostrophic approximation. It involves averages taken along Taylor surfaces, which in our geometry are straight line segments parallel to the rotation axis. Taylor's solvability condition in the present geometry is derived in Appendix A.

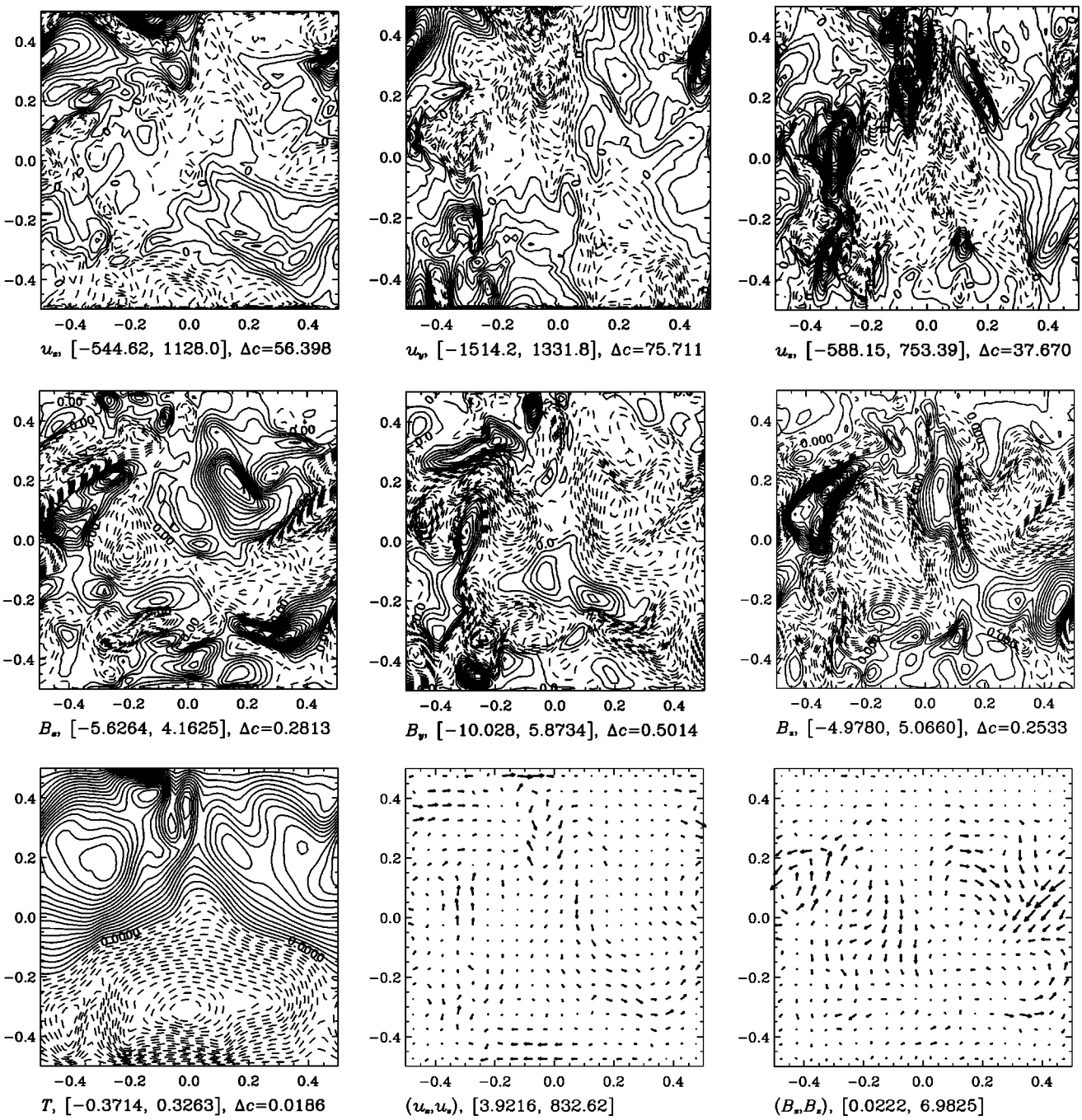

FIG. 12. Snapshot of the velocity (u_x,u_y,u_z) (first row), the magnetic field (B_x,B_y,B_z) (second row), and the temperature T (lowermost left plot) in the $y=0$ plane for the dynamo at $E=1\times10^{-5}$. Positive (negative) values are depicted by solid (dashed) contour lines. The interval below the each panel indicates the range of the displayed quantity. The contour level separation is denoted by Δc. The two vector field plots are (u_x,u_z) (left) and (B_x,B_z) in the $y=0$ plane. The interval below these plots gives the range of arrow lengths. The snapshot is taken at the same time as for the magnetic part of Fig. 9.

In spherical geometry, the Taylor surfaces are cylinders coaxial with the rotation axis. Some kinematic dynamos satisfy Taylor's condition directly, examples being given by Jault and Cardin [15]. The spherical geometry allows a symmetry (rotation by π about an equatorial axis) that preserves the Taylor cylinders. Kinematic dynamos with this symmetry produce magnetic fields that are directly in a Taylor state. In our geometry the inclined rotation axis prevents a symmetry that preserves the Taylor line segments. In general, a coupling between the geostrophic flow and magnetic field is needed in order to drive the magnetic solution towards a kinematic Taylor state.

A measure of Taylorization [16] is given in Appendix A. The results are summarized in Fig. 16 that displays a decreasing (differential) Taylorization. The Taylorization seems to scale as $E^{1/6}$ at $E=1\times10^{-5}$. Thus the magnetic solution

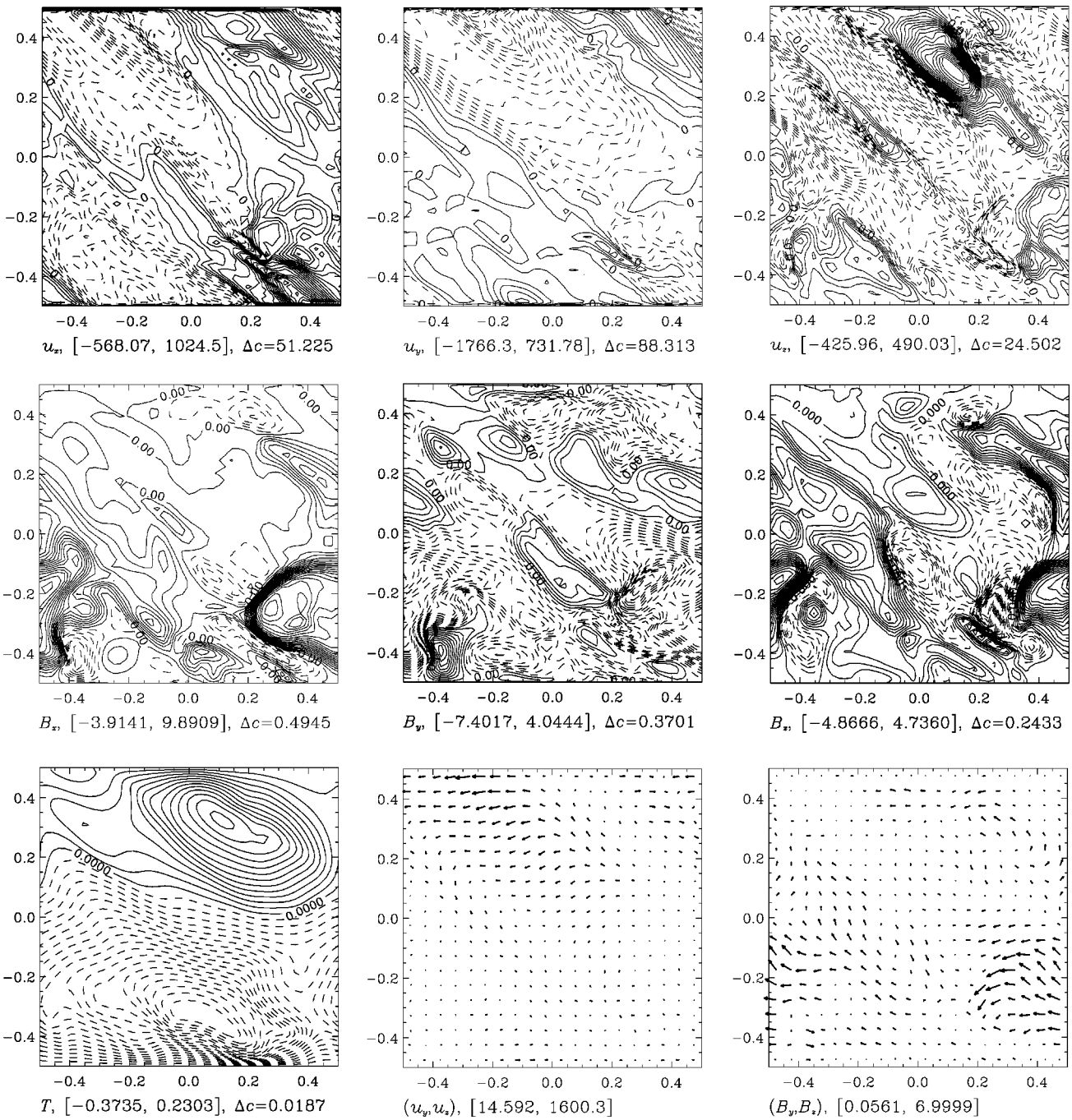

FIG. 13. Similar to Fig. 12, but for the $x=0$ plane. The two vector field plots are (u_y,u_z) (left) and (B_y,B_z) in the $x=0$ plane.

is clearly approaching a Taylor state in the range $E \in [10^{-5},10^{-4}]$. For the sequence II runs, we find that the Taylorization scales as $E^{1/3}$ at $E=1\times10^{-5}$.

The ratio between the geostrophic and total kinetic energy of the dynamos is about 14%, 13%, 14%, and 19%, in decreasing Ekman number order. The geostrophic velocity is somewhat influenced by the Lorentz force since the geostrophic energy is 22%, 25%, 24%, and 36% of the total kinetic energy for nonmagnetic convection at the same points in parameter space. The geostrophic velocity alone cannot produce a Taylor state. In the classical Malkus-Proctor scenario, it merely drives the solution towards kinematic Taylor states. Thus for saturated Taylor states we expect the ageostrophic velocity to be a significant part of the flow, which is clearly confirmed in our case. However, even if the geostrophic velocity is a minor part of the flow, it seems to be needed, by an approximately constant relative amount, in the production of approximate Taylor states.

E. 2.5D model

The 2.5D technique allows investigation of longer model time intervals. We keep the x and z resolutions as in the 3D

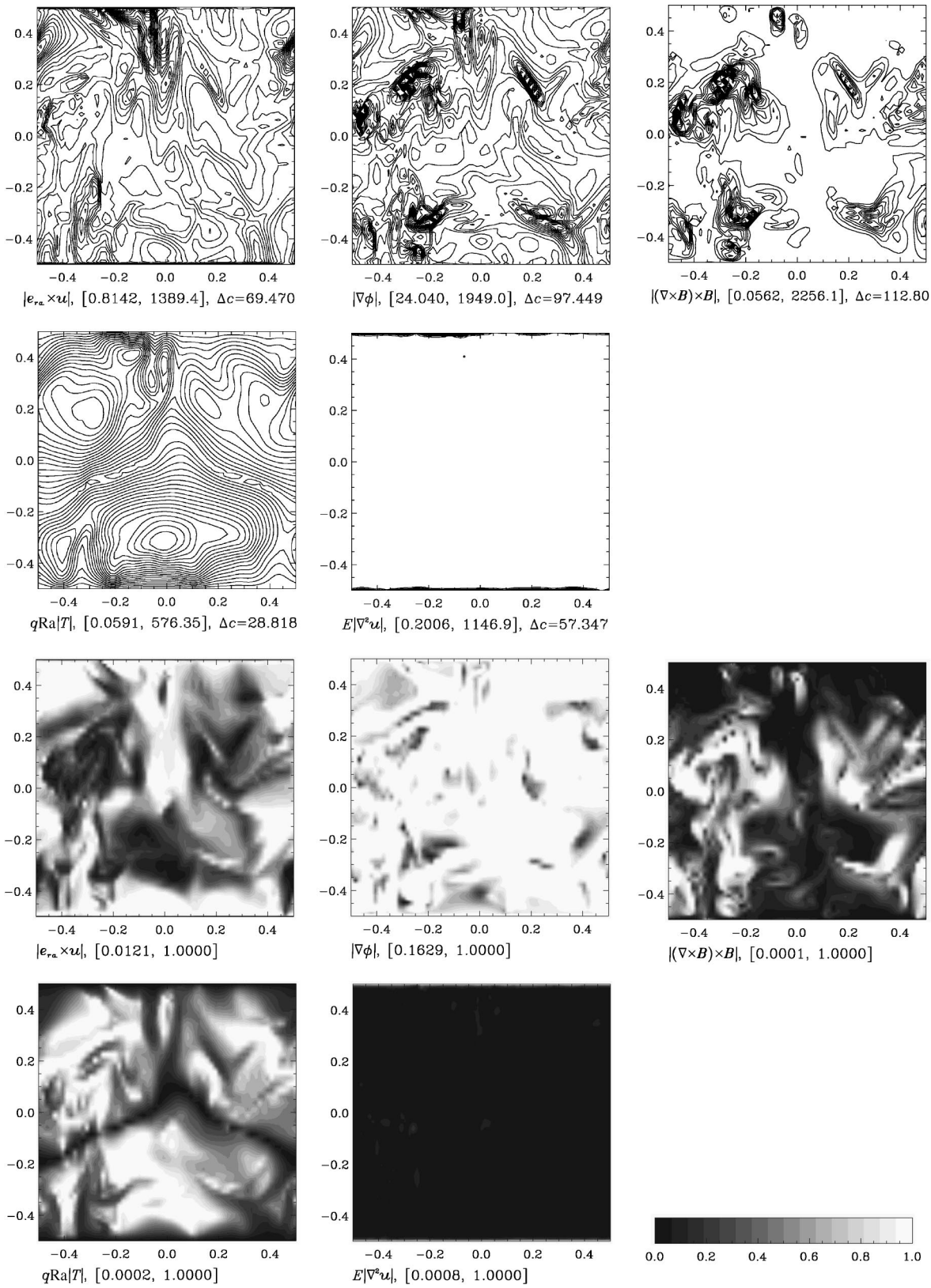

FIG. 14. Snapshot of the various forces in the $y=0$ plane for the dynamo at $E=1\times10^{-5}$. The first two rows are contour plots of the absolute value of the forces. They are (in row major order) Coriolis, pressure, Lorentz, buoyancy, and viscous forces. The two lowermost rows show the relative strengths of the forces (displayed in the previous order). The intensity at each point scales linearly with the strength of the force relative to the strongest force at this point. Thus the strongest force is white. The snapshot is taken at the same time as Fig. 12.

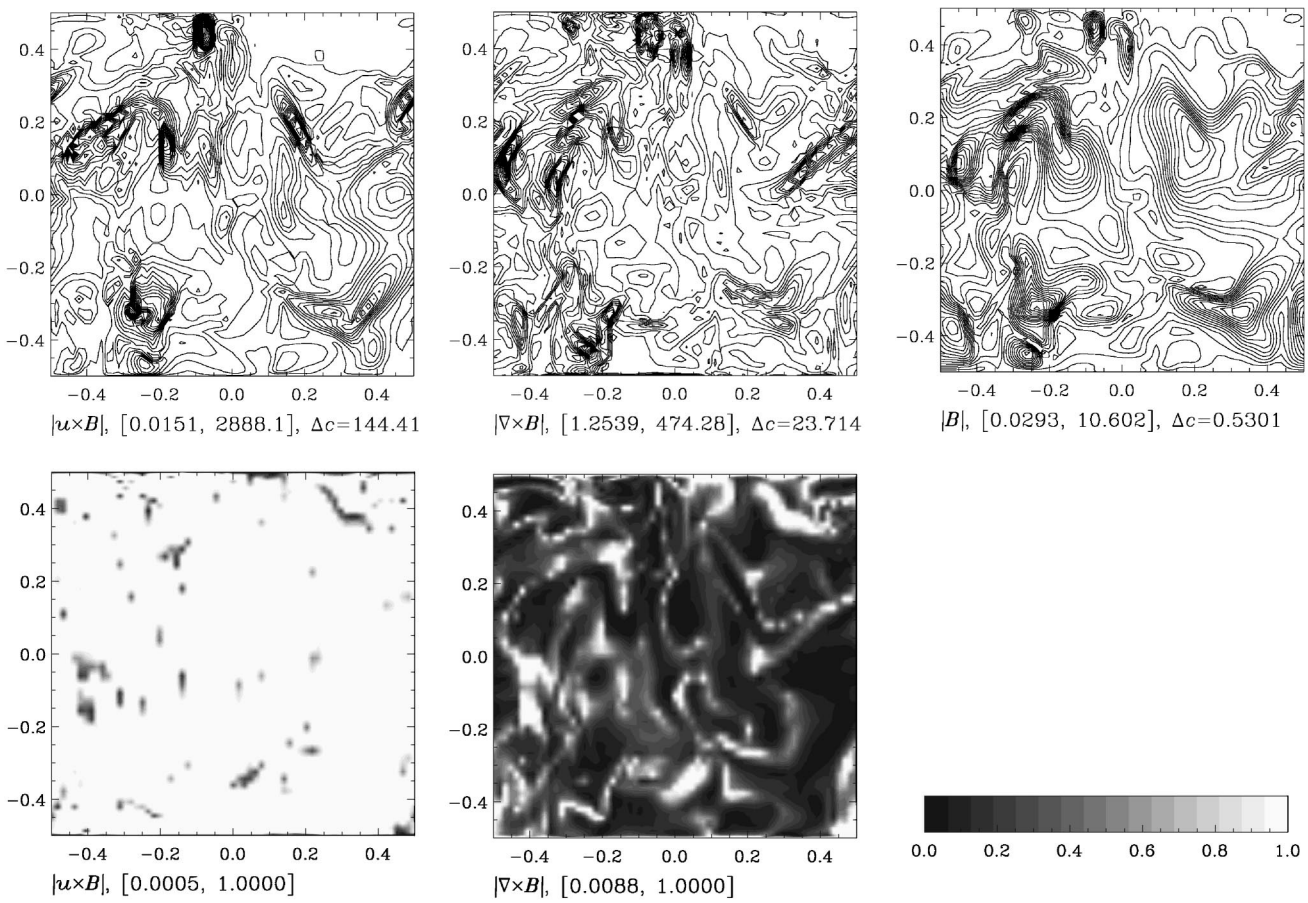

FIG. 15. Snapshot of $|\mathbf{u}\times\mathbf{B}|$, $|\nabla\times\mathbf{B}|$, and $|\mathbf{B}|$ in the $y=0$ plane for the dynamo at $E=1\times10^{-5}$ (first row). The second row displays the relative strength between $|\mathbf{u}\times\mathbf{B}|$ and $|\nabla\times\mathbf{B}|$ by the method used in Fig. 14. The snapshot is taken at the same time as Fig. 12.

case, see Sec. V A, but reduce the number of y modes to 4 dealiased modes. In view of recent 2.5D successes, e.g., Ref. [4], 2.5D results should not be rejected automatically. Since, in addition, the nonmagnetic case has been designed to give good 2.5D results, we may put some confidence in the magnetic case as well.

The four dynamos of Sec. V A have been integrated in a 2.5D setting. At $E=10^{-4}$ the initial state is taken as a truncated saturated state of the 3D integration. The solution spans three magnetic diffusion times, see Fig. 17. It displays a strong time dependence. For large periods of time, the Elsasser number stays well above 1. However, during relatively short intervals, the magnetic field becomes very weak. The nonmagnetic convection mode is restored, typically when the

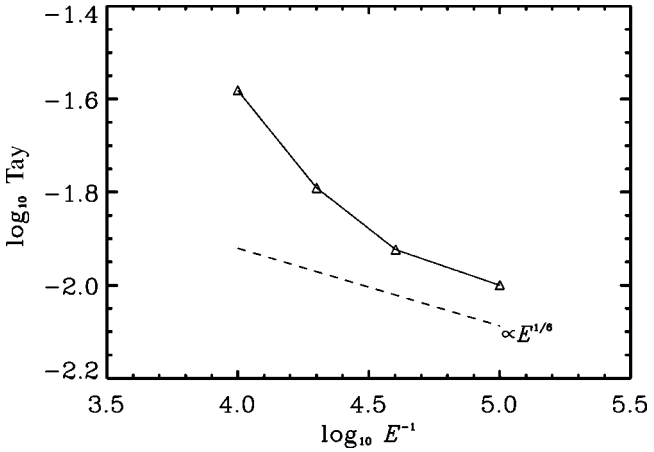

FIG. 16. Taylorization as a function of the Ekman number. The dashed line represents an $E^{1/6}$ scaling.

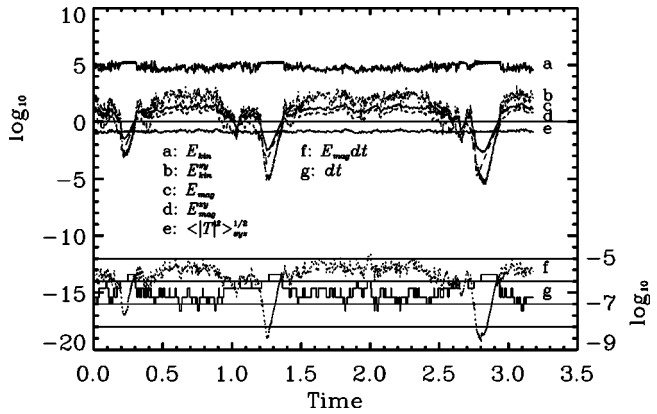

FIG. 17. A 2.5D dynamo at $E=1\times10^{-4}$. The linestyle definitions are the same as in Fig. 6 applied at the final state.

Elsasser number decreases below 1, and then kinematic dynamo action drives the magnetic field back to a state with Elsasser number above 1.

We employ the snapshot method described in Sec. V A starting at $E=5\times10^{-5}$. We then reduce the Ekman number down to 5×10^{-6} in three steps. The magnetic energy E_{mag} in [4,10]. At $E=5\times10^{-6}$, some features in this 2.5D example are comparable with the 3D model. The geostrophic component is about 28% of the total kinetic energy. The temperature scaling is compatible with $O(E^{-1/12})$ and the kinetic energy is $O(E^{-2/3})$. However, the magnetic energy scaling is $O(E^{-1/2})$ and the Taylorization scales as $O(E^{4/3})$. The latter indicates that the solution is moving faster towards a Taylor state than the 3D model. Thus it seems that the dynamical part of the 2.5D integration is comparable with the 3D model, but that the magnetic properties differ significantly.

VI. CONCLUSIONS

In the $E\to0$ asymptotic regime, the leading order features of the flow are not influenced by viscosity, except within thin viscous boundary layers. A number of indicators suggest that we have achieved this asymptotic regime for moderate Rayleigh number rotating convection-driven dynamos with an Ekman number below 10^{-4}.

A crude indicator consists of comparing the strength of the viscous force with other forces. For $E<10^{-4}$, the magnetostrophic approximation applies to good accuracy almost everywhere except within the Ekman layers. This comparison also shows that a MAC balance is maintained within the bulk.

As we have demonstrated in this paper, the structure of the kinetic energy spectra provides a good indicator of the asymptotic regime. In these spectra we obtain scale separation between the magnetic and nonmagnetic cases only when $E<10^{-4}$. This scale separation must be present in order to conclude that the leading order effects on the bulk flow are not influenced by viscosity. We note that at $E=1\times10^{-4}$, an Elsasser number of order $O(10)$ is not sufficient to produce a scale separated solution.

In the asymptotic regime, Taylor's constraint is only satisfied approximately. Our 3D example clearly demonstrates that differential Taylorization occurs when $E<10^{-4}$. This does not imply that the magnetic field is either simple or steady. Rather remarkably, the flow continually adjusts to generate an approximate Taylor solution. Violation of the Taylor's constraint influences the geostrophic velocity, which in turn adjusts the magnetic solution towards a Taylor state. The strength of this feedback mechanism is approximately constant for $E<10^{-4}$.

A fourth asymptotic regime indicator is provided by order of magnitude estimates. Based on the MAC balance we estimate the kinetic energy, a typical length scale of the magnetic field, and the frozen-flux approximation. We find that these estimates are consistent with the numerical results at $E=1\times10^{-5}$.

The above indicators either start to appear or are already present when $E\in[10^{-5},10^{-4}]$. Thus it seems likely that the next decade, $E\in[10^{-6},10^{-5}]$, which at present is too expensive numerically to be explored extensively, will be well within the asymptotic regime. Unfortunately, current spherical convection-driven dynamo models are generally not yet in the asymptotic regime, which is hard to achieve because of the high resolution required and the small time step needed to maintain stability. Because of the large computing requirement, it is natural to look for simplified models. Our 2.5D model with four modes in the y direction is one such model. The results suggest that 3D and 2.5D results are similar in many respects, e.g., time series of quantities like kinetic energy, magnetic energy, and temperature are quite similar. However, it seems that the magnetic properties of the solutions are somewhat different and that 3D models are required to describe these fully.

Finally, an important result is that at low viscosity, small-scale structures become increasingly important relative to the large-scale components. This feature provides some basis for the snapshot method, but since the small-scale structures operate on faster time scales, it also raises the question whether the $\mathrm{Ro}\to0$ asymptotic regime becomes narrower at low viscosity. If so, future low Ekman number simulations face an additional challenge. In order to establish the extent of the $\mathrm{Ro}\to0$ regime, inertial acceleration has to be taken into account and the solutions will have to be characterized along an extra dimension of parameter space.

ACKNOWLEDGMENTS

This work was supported by PPARC Grant No. GR/L40922. The computational work was performed on the IBM SP2 computing facility at the University of Exeter, and on the cluster of the U.K. MHD consortium (Compaq Alpha EV6). We would also like to thank A. M. Soward for useful discussions.

APPENDIX A: TAYLOR'S CONDITION

In order to derive the solvability condition for Eq. (8), we rotate the coordinate system an angle θ about the x axis. Denoting the new coordinates by (x,y,z), Eq. (8) becomes

$$\mathbf{e}_z\times\mathbf{u}=-\nabla\phi+\mathbf{G}. \tag{A1}$$

The upper and lower boundaries are parametrized by

$$(x,y)\to(x,y,f(x,y)),(x,y)\to(x,y,g(x,y)), \tag{A2}$$

respectively. Thus perpendicular outward directed vectors are, e.g., $\mathbf{n}_T=-\nabla f+\mathbf{e}_z$ and $\mathbf{n}_B=\nabla g-\mathbf{e}_z$. In the following, we impose no-penetration boundary conditions,

$$\mathbf{n}_T\cdot\mathbf{u}_T=0,\quad \mathbf{n}_B\cdot\mathbf{u}_B=0. \tag{A3}$$

We may find a necessary solvability condition for Eq. (A1) by taking the curl and average

$$\mathbf{n}_T\cdot\langle\nabla\times\mathbf{G}\rangle=0, \tag{A4}$$

where $\langle \cdots \rangle$ denotes the average along the z axis. Equation (A4) turns out to be sufficient as well. To prove the latter we construct a solution [17],

$$\mathbf{u} = -\nabla \times \mathbf{Q}, \quad \phi = \mathbf{e}_z \cdot \mathbf{Q}, \tag{A5}$$

$$\mathbf{Q} = \frac{1}{2}\left[\int_g^z \mathbf{G}\, dz' - \int_z^f \mathbf{G}\, dz' \right]. \tag{A6}$$

Since

$$(\nabla \times \mathbf{Q})_T = \frac{1}{2}[\langle \nabla \times \mathbf{G} \rangle + \mathbf{n}_T \times \mathbf{G}_T - \mathbf{n}_B \times \mathbf{G}_B], \tag{A7}$$

$$(\nabla \times \mathbf{Q})_B = \frac{1}{2}[-\langle \nabla \times \mathbf{G} \rangle + \mathbf{n}_T \times \mathbf{G}_T - \mathbf{n}_B \times \mathbf{G}_B], \tag{A8}$$

the boundary conditions (A3) reduce to Eq. (A4). Thus Eq. (A1) may be solved if and only if Taylor's condition (A4) is satisfied. The buoyancy force is perpendicular to the boundaries, hence only the magnetic field is subjected to Taylor's condition.

Let us consider the form of the geostrophic velocity. Solutions $(\mathbf{u}, \phi)$, $\nabla \cdot \mathbf{u} = 0$, to Eq. (A1) differ by a component that satisfies the homogeneous part,

$$\mathbf{e}_z \times \mathbf{u} = -\nabla \phi. \tag{A9}$$

It is clear that a solution $(\mathbf{u}, \phi)$, $\nabla \cdot \mathbf{u} = 0$, to Eq. (A9) is z independent. Let $\phi(x,y)$ be given. Then $\mathbf{u} = \mathbf{n}_T \times \nabla \phi$ is the unique incompressible velocity. If on the other hand, $\mathbf{u}(x,y)$, $\nabla \cdot \mathbf{u} = 0$, is given we may find a pressure ϕ since $\nabla \times (\mathbf{e}_z \times \mathbf{u}) = 0$. Thus the velocity part of a solution to Eq. (A1) is unique when the geostrophic component,

$$\mathbf{u}_G = -\langle \mathbf{n}_T \times (\mathbf{e}_z \times \mathbf{u}) \rangle, \tag{A10}$$

is restricted to zero. The geostrophic velocity has zero divergence, since

$$\nabla \cdot \langle \mathbf{v} \rangle = \langle \nabla \cdot \mathbf{v} \rangle - \mathbf{n}_T \cdot \mathbf{v}_T - \mathbf{n}_B \cdot \mathbf{v}_B. \tag{A11}$$

Let us return to the previous coordinate system. Taylor's condition (A4) then becomes

$$\mathbf{e}_z \cdot \langle \nabla \times \mathbf{G} \rangle_{ra} = 0, \tag{A12}$$

where $\langle \cdots \rangle_{ra}$ is the average along the rotation axis. We put $h = \mathbf{e}_z \cdot \nabla \times \mathbf{G}$. We may define a scalar, the Taylorization Tay, to indicate how well the Taylor's condition is satisfied

$$\mathrm{Tay} = \frac{\langle |\langle h \rangle_{ra}|^2 \rangle_{xy}}{\langle \langle |h|^2 \rangle_{ra} \rangle_{xy}}. \tag{A13}$$

Expanding

$$h = \sum_{l,m}^{n} A_{lm}^n e^{i2\pi(lx+my)} T_n(2z), \tag{A14}$$

we find that

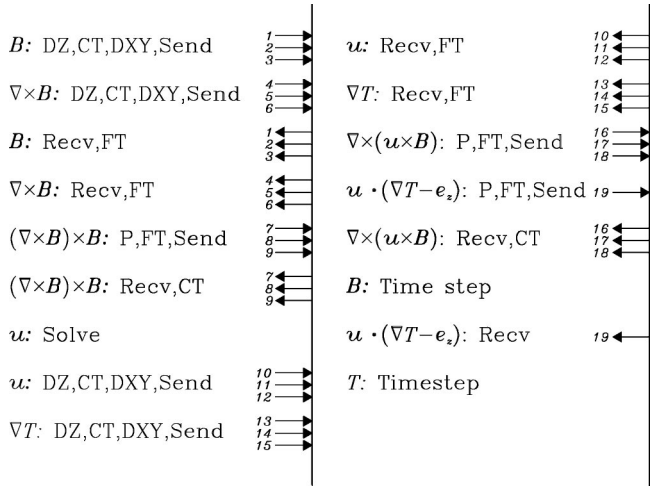

FIG. 18. Program flow and interprocess communication scheme. The vertical lines indicate the network between processes. The required transpositions of distributed arrays have been numbered 1–19. The abbreviations are as follows. *DXY*: x and y derivatives, *DZ*: z derivatives, FT: Fourier transforms, CT: Chebyshev transforms, P: products of nonlinear term, Send (Recv): either a blocking all-to-all MPI call (no operation) or a set of point-to-point nonblocking MPI sends (receives) (note that in the former case the number of calls may be reduced to 4, see text).

$$\mathrm{Tay} = \frac{\sum_{l,m} \left| \int_{-1/2}^{1/2} e^{-i2\pi m t \tan\theta} A_{lm}(t)\, dt \right|^2}{\sum_{l,m} \int_{-1/2}^{1/2} |A_{lm}(t)|^2\, dt}, \tag{A15}$$

where $A_{lm}(t) = \Sigma_n A_{lm}^n T_n(2t)$. The geostrophic velocity component of $\mathbf{u}$ is

$$\mathbf{u}_G = -\frac{\langle \mathbf{e}_z \times (\mathbf{e}_{ra} \times \mathbf{u}) \rangle_{ra}}{\mathbf{e}_z \times \mathbf{e}_{ra}}. \tag{A16}$$

APPENDIX B: PARALLELIZATION OF PROGRAM

The computer program may run on parallel architectures by use of mixed MPI/OpenMP. The two communication protocols may be activated independently. This allows communication to be optimized on different types of parallel computers: clusters, SMPs, and SMP clusters. To simplify the description below we restrict it to the pure MPI case.

The required communication between processors occurs when (i) performing transforms between spectral and physical space, (ii) evaluating global quantities such as energy, and (iii) loading and saving states. The state monitoring is usually kept to a minimum. Thus only optimization of (i) is important for program performance. The third index of the 3D arrays is distributed among the processors, and transformation between spectral and physical space involves, for each value of the second index, a matrix transposition of distributed 2D arrays. Hence each processor has to send data to itself and every other processor.

Figure 18 illustrates the program flow. For example, the first step evaluates the toroidal/poloidal/mean field expanded

magnetic field in horizontal Fourier space and on the vertical collocation mesh (the calculations are z derivatives, followed by Chebyshev transforms, and completed by evaluation of x and y derivatives). The three distributed vector components of the magnetic field are then transposed. In the third step, the magnetic field is evaluated on the horizontal Fourier grid by Fourier transforms.

The communication may be performed in three different ways, see Fig. 18.

(i) Each communication is a blocking all-to-all MPI call. The performance of this scheme has been tested on an IBM SP2 using up to 16 processors. The scaling is good, e.g., at resolution $32\times4\times48$ a speedup factor of 13.6 is obtained on 16 processors. Performance is best, of course, when the number of processors divide the sizes of the distributed dimensions.

(ii) The 19 communications can be collected into four large packages: (1–6), (7–9), (10–15), and (16–19). This method may use the network bandwidth more efficiently. However, on the SP2 it turns out that the performance only increases slightly.

(iii) Each communication is a set of nonblocking point-to-point MPI calls allowing computation and communication to be overlapped. The principle is to send (receive) as early (late) as possible. A large part of the time spent on the nonlinear terms is used on Fourier or Chebyshev transforms. We may overlap these transforms with nonblocking communication as shown in Fig. 18. This method has the potential to eliminate the communication overhead all together. However, the hardware must support concurrent computation and communication in order to gain extra performance.

A performance comparison between the above three communication schemes favors method (ii) marginally on the SP2.

[1] U. Christensen, P. Olson, and G.A. Glatzmaier, Geophys. J. Int. **138**, 393 (1999).
[2] G.A. Glatzmaier and P.H. Roberts, Phys. Earth Planet. Inter. **91**, 63 (1995).
[3] K. Zhang and C.A. Jones, Geophys. Res. Lett. **24**, 2869 (1997).
[4] G.R. Sarson, C.A. Jones, and A.W. Longbottom, Geophys. Astrophys. Fluid Dyn. **88**, 225 (1998).
[5] C.A. Jones and P.H. Roberts, J. Fluid Mech. **404**, 311 (2000).
[6] H.P. Greenspan, *The Theory of Rotating Fluids* (Cambridge University Press, Cambridge, England, 1968).
[7] S. Chandrasekhar, *Hydrodynamic and Hydromagnetic Stability* (Clarendon Press, Oxford, 1961).
[8] M.G. St. Pierre, *Solar and Planetary Dynamos* (Cambridge University Press, Cambridge, England, 1993).
[9] P.C. Matthews, Proc. R. Soc. London, Ser. A **455**, 1829 (1999).
[10] P.H. Roberts and G.A. Glatzmaier, Philos. Trans. R. Soc. London, Ser. A **358**, 1109 (2000).
[11] A. Brandenburg, Astrophys. J. **550**, 824 (2001).
[12] M.R. Walker, C.F. Barenghi, and C.A. Jones, Geophys. Astrophys. Fluid Dyn. **88**, 261 (1998).
[13] K. Zhang and G. Schubert, Annu. Rev. Fluid Mech. **32**, 409 (2000).
[14] J.B. Taylor, Proc. R. Soc. London, Ser. A **274**, 274 (1963); D.R. Fearn and M.R.E. Proctor, Geophys. Astrophys. Fluid Dyn. **67**, 117 (1992).
[15] D. Jault and P. Cardin, Phys. Earth Planet. Inter. **111**, 75 (1999).
[16] A.P. Anufriev, I. Cupal, and P. Hejda, Geophys. Astrophys. Fluid Dyn. **79**, 125 (1995).
[17] A.M. Soward (private communication).